Urol Res (2011) 39:259–267
DOI 10.1007/s00240-010-0343-9

ORIGINAL PAPER

Investigation of the microstructure and mineralogical composition of urinary calculi fragments by synchrotron radiation X-ray microtomography: a feasibility study

Jozef Kaiser · Markéta Holá · Michaela Galiová · Karel Novotný · Viktor Kanický · Petr Martinec · Jiří Ščučka · Francesco Brun · Nicola Sodini · Giuliana Tromba · Lucia Mancini · Tamara Kořistková

Received: 13 April 2010 / Accepted: 4 November 2010 / Published online: 16 December 2010

Abstract The outcomes from the feasibility study on utilization of synchrotron radiation X-ray microtomography (SR-μCT) to investigate the texture and the quantitative mineralogical composition of selected calcium oxalate-based urinary calculi fragments are presented. The comparison of the results obtained by SR-μCT analysis with those derived from current standard analytical approaches is provided. SR-μCT is proved as a potential effective technique for determination of texture, 3D microstructure, and composition of kidney stones.

Keywords Computed microtomography · Synchrotron radiation · Urinary calculi · Texture · Microstructure

J. Kaiser (✉) · M. Galiová
Institute of Physical Engineering, Faculty of Mechanical Engineering, Brno University of Technology, Technická 2896/2, 616 69 Brno, Czech Republic
e-mail: kaiser@fme.vutbr.cz

M. Holá · M. Galiová · K. Novotný · V. Kanický
Department of Chemistry, Faculty of Science, Masaryk University, Kotlářská 2, 611 37 Brno, Czech Republic

P. Martinec · J. Ščučka
Institute of Geonics, Academy of Sciences, Studentská 1768, 708 00 Ostrava-Poruba, Czech Republic

J. Kaiser · F. Brun · N. Sodini · G. Tromba · L. Mancini
Sincrotrone Trieste S.C.p.A., Strada Statale 14, km 163.5 in AREA Science Park, Basovizza, 34149 Trieste, Italy

T. Kořistková
Laboratory Specializing in Urinary Stones Analyses, Calculi®, Vránova 172, P.O.Box 20, 621 00 Brno, Czech Republic

Introduction

Among all types of urinary calculi that are affecting the populations of industrialized countries, the frequency of calcium stone is 70–80% [1]. The primary component of 70–80% of calcium stones in the US is the calcium oxalate [2, 3].

The susceptibility of the calcium oxalate stones to the shock wave (SW) lithotripsy [4], which is one of the methods of nephrolithiasis therapy, is varying dramatically depending on their fragility. Some homogenous and compact calculi being very resistant, and others, with heterogeneous and less compact structure are quite fragile [5]. Modeling and optimization of SW lithotripsy need the knowledge of treated stones mineral composition and structure [6]. The study of urolithiasis requires not only identification of constituents and minerals, but also knowledge about their internal texture and structure. Current methods of chemical analysis (AAS, ICP-OES, ICP-MS), which are based on determination of analytes after sample dissolution [7], provide only information on bulk composition of uroliths. It was already found at initial mineralogical studies of urolith thin sections by means of optical microscopy in polarized light that uroliths exhibit distinct concentric texture, which indicates dynamics of urolith evolution. Concentric texture is manifested by zonation of mineralogical composition and amorphous constituents as well as by mineral grains size and degree of perfection of their crystallographic arrangement [8]. Recent studies underlined the necessity to perform analysis of urinary calculi at the mesoscopic scale. Close relationship between the stone morphology and crystallite organization at the mesoscopic level and the effectiveness of extracorporeal SW lithotripsy was shown, e.g., in [9]. Another study [10] using SEM confirmed a crystalline structure in

the primary hyperoxaluria type 1 stone that was distinct from that of the common type of whewellite stone. Routine X-ray examination of patients made it also possible to distinguish the urinary calculi zonation to some extent [11]. Computed tomography (CT) was employed for determination of location, size and shape of uroliths [12, 13], and micro CT (μCT) was proved useful for urolith structure imaging and determination of its composition [14]. Spiral CT was demonstrated to be an efficient tool for detection of uroliths of the size down to 1 mm [15, 16]. Dual-energy multidetector computed tomography was used for the study of composition [17–20] and surface area [21] of uroliths.

In this work, synchrotron radiation microtomography (SR-μCT) was investigated as a potential effective technique for the determination of texture, microstructure, and mineralogical composition of kidney stones. Even if this technique most probably can be hardly applied for analysis of the human kidney stones in routine basis, it can give valuable information, e.g., for rare, special or abnormal samples before the routine analysis. Non-destructive mapping of the urinary stones' inner structure together with the possibility of mineral composition identification based not only on X-ray attenuation values, but also using the contrast due to the phase modulation allow selecting the proper cross-sections of interests across the samples, where further analysis using the more routine approaches can be realized. Similar methodology was recently successfully applied for another bio-minerals, e.g., to visualize at three-dimensional (3D) level, microvascular networks for the first time with no need for contrast agents, and to extract quantitative structural data in a bone-engineered construct implanted for 24 weeks in a mouse [22]. When compared to standard histology, pseudo-holotomography allowed a previously unavailable 3D resolution of the vessels, which in turn appeared more clearly visible.

Going back to urinary calculi samples, the non-destructive high-resolution visualization of the sample volume is important also for the development and successful utilization of analytical methods that can measure elements' concentration at appropriate spatial resolution, similar to the urinary calculi bio-mineral structures, as e.g., laser-induced breakdown spectroscopy (LIBS) [23, 24] and laser-ablation inductively coupled mass spectrometry/optical emission spectrometry LA-ICP-MS/OES [25, 26]. In order to apply these techniques effectively, it is advantageous to know the structure of the entire investigated sample before the LIBS or LA-ICP-MS/OES analysis and/or to investigate the parameters of the laser-ablation crater or laser-ablation pattern after the chemical composition mapping [27].

The SR-μCT experiments were performed at the SYRMEP beamline of the Elettra Synchrotron Light Laboratory in Trieste (Italy). Thanks to the SYRMEP station features such as the energy range available, the small angular source size and the large section of the X-ray beam it is possible to obtain not only a high spatial resolution on macroscopic samples, but also to exploit the transverse coherence properties of the X-ray beam [28, 29]. In particular, SR-μCT measurements in parallel beam geometry allow reconstructing different regions of large-scale objects (centimeter sized) at high spatial resolution (of the order of a few microns) and with beam artifacts strongly reduced with respect to the use of polychromatic conventional sources [30]. Moreover, using phase-contrast μCT also very small variations in density and chemical composition could be visualized within a given sample, and then different minerals could be imaged in the sample matrix, due to a contrast enhancement at the boundary between the different mineral phases. This will allow not only distinguishing the areas with different chemical composition within the same sample but also a non-destructive localization of distinct concentric texture inside the stone.

Materials and methods

Sample characterization

Overall mineralogical composition of selected fragments of calcium oxalate-based urinary calculi was determined by means of: (1) optical microscopy both in plane polarized light and by crossed nicols; (2) infrared spectroscopy (IRS); (3) scanning electron microscopy (SEM) and (4) elemental analysis by ICP-MS.

For three selected concentric urinary calculi (Fig. 1), common basic structure is observed, which consists of a markedly crystalline surface crust flanking a central part. Urinary stone fragments with central part having a different texture, ranging from the more compact (sample 10371, Fig. 1a) up to rather heterogeneous (sample 11847, Fig. 1c) were selected. In the samples the following minerals were determined: Ca-oxalates (whewellite and weddellite) and apatite.

Sample no. 10371 (Table 1) is an oval urinary calculus of brownish white color with fine-grained surface. Cross-section comprises homogenous structure with visible zonation. The nucleus is in the geometric center of the stone and consists of whewellite. The sample contains whewellite and on the surface traces of weddellite (less than 5%).

Sample no. 11727 (Table 1) is an oval urinary calculus of beige color with mulberry surface. On the surface is whewellite, covered with apatite. Cross-section shows concentric layers of whewellite with gaps in several places. There is no clearly evident nucleus. Sample contains whewellite with traces of apatite.

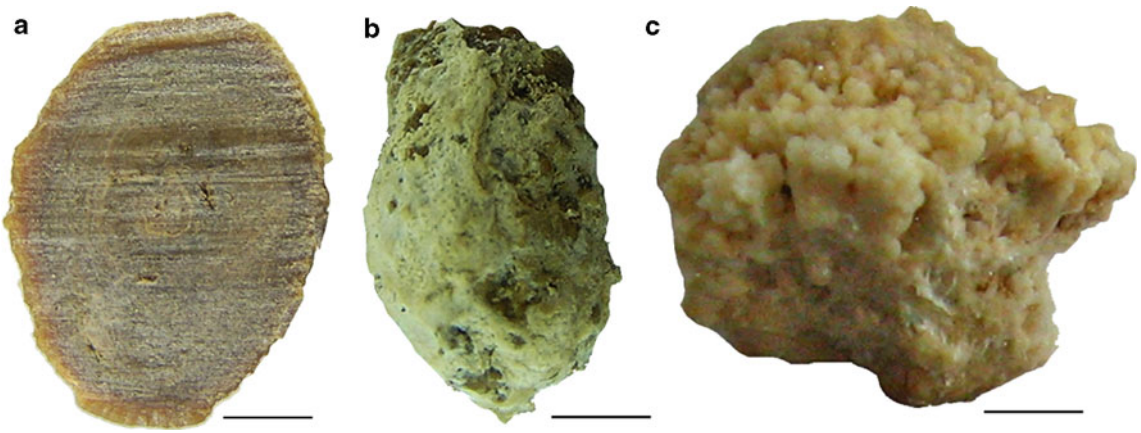

Fig. 1 The analyzed urinary calculi fragments no.: **a** 10371, **b** 11727 and **c** 11847. The *bars* have a length of 2 mm

Table 1 Data of patients and the analyzed urinary calculi [31]

Sample no.	Patient's sex	Birth year	Surgery year	Diagnose	RTG contrast	Localization	Side	Origin
10371	Female	1959	2005	N20.0	Yes	Calyx	Right	Surgical
11727	Female	1954	2007	N20.0	Yes	Pelvis	Left	Surgical
11847	Male	1951	2007	N20.0	Yes	Calyx	Right	Surgical

Sample no. 11847 (Table 1) is a crystalline urinary calculus of caramel brown color with rough porous surface indistinctly granular with coarse crystalline incremental zone constituted by oxalate crystals in the surface crust. Central crystalline part comprises oxalates with apatite. Sample contains in average 45% of whewellite, 20% of weddellite, and 35% of apatite.

SR-μCT of the investigated samples

The SR-μCT measurements on urolith samples were performed at the SYRMEP beamline of Elettra. The X-ray source is a bending magnet and the beamline provides, at a distance of about 23 m from the source, a monochromatic, laminar-section X-ray beam with a maximum area of about 160×5 mm^2 at 20 keV. The monochromator is based on a double Si(111) crystal system working in Bragg configuration that can be tuned in an energy range of 8.3–35 keV with an energy-resolving power of about 10^{-3}.

Due to the small angular source size and the simple design of the beamline, the X-ray beam in the experimental hutch is characterized by a good level of spatial coherence (transversal coherence length of about 10 μm at 15 keV) allowing to perform phase-contrast imaging using simple free space propagation [32]. Phase-contrast imaging enhances the visibility of objects modifying the local phase of the transmitted X-ray beam (for instance inclusions, pores, interfaces between regions with different mass density) and this contrast can be revealed simply varying the sample-to-detector distance.

For SR-μCT experiments the samples have been mounted on a high-resolution rotation stage and illuminated with a monochromatic radiation. A water cooled Photonics Science Hystar 16-bit CCD camera was used as detector. The camera head consists of a high-resolution 2048×2048 pixels, full frame CCD imager, which is directly bonded to a tapered fiber optic. Two different detector configurations were used in our experiments. In configuration (A) samples were imaged using a 14 μm pixel size with an active input area of 28×28 mm imaged on the sensor; in configuration (B) an effective pixel size of 3.85 μm was employed corresponding to a field of view of 8×8 mm.

Images have been recorded with the CCD camera located at a distance d of 50 cm from the sample. The sample-to-detector distance was chosen in order to work in the edge-detection regime for phase-contrast μCT [32].

For each tomographic scan 1,440 projections of the sample were acquired for equally spaced rotation angles over a total rotation of 180°; the tomographic scans lasted from 1 h to a maximum of 5 h depending on the ring current, sample absorption, and pixel size of the detector. The measurement parameters were previously optimized by imaging several samples under different conditions.

After data acquisition, the SYRMEP Tomo Project software code based on the filtered back-projection

algorithm [33] and custom-implemented at Elettra by F. Montanari [34], was used to reconstruct the 3D images of the sample by series of 2D slices. The resulting 3D digital volumes were rendered using the commercial software VGStudio MAX 2.0.

Principle of assignment of image structure to particular minerals: interpretation of reconstructed SR-μCT slices

The starting point for interpretation of SR-μCT slices of urinary calculi is given by information on mass density values of minerals and other constituents. Besides, morphology of grains, habitus of mineral crystals and overall mineralogical composition of concrements are indispensable for proper assignment of particular zones in SR-μCT slices to corresponding structures in a urinary calculus. The chemical formulas, mass density values and crystalline systems of minerals contained in investigated samples are presented in Table 2.

In fact, in the slices reconstructed from SR-μCT experiments the gray level values are inversely proportional to the mass density values of irradiated matter. The mass density value of a particular mineral is employed for defining its corresponding area of occurrence in the SR-μCT slices according to brightness of a relevant image pixel. Consequently, particular minerals manifest themselves in a slice as areas characterized by various gray levels. A particular gray level is given by an interval of intensity values of pixels (or voxels).

The simplest and fastest way to reveal some information about the texture of the sample in the investigated slice is to use lookup-tables in order to emphasize the differences between crystals ("Sample 11847"). However, it should be noted that the use of lookup tables is always sample specific. They can give some fast and preliminary information for some kind of samples or, e.g., a specific type of texture present. In general, they cannot be used for quantitative analysis. Here the slices in different lookup-tables were created using the ImageJ software [35].

Table 2 Description of minerals present in the investigated samples

Mineral	Formula	Mass density [g cm^{-3}]	Form
Whewellite	$CaC_2O_4{\cdot}H_2O$	2.23	Monoclinic crystals.
Weddellite	$CaC_2O_4{\cdot}2H_2O$	1.94	Tetragonal pyramids.
Apatite	$Ca_5(PO_4,CO_3)_3(OH)$	3.04	Carbonate-hydroxylapatite, hexagonal, prismatic crystals.

As shown in Table 1, the whewellite and weddellite minerals have a very close mass density and chemical composition. So the differences in the gray levels related to these materials are very small giving a weak contrast in the μCT images acquired in absorption mode. This can also be verified calculating the mass attenuation coefficients μ/ρ of the two minerals. These parameters calculated by WinXCom software [36–38] for energy 28 keV (utilized for most of the measurements) are 1.51 and 1.64 cm^2 g^{-1} for weddellite (WD) and whewellite (WH), respectively. Using the tabulated mass density values for these two crystals (Table 2) the difference in linear attenuation coeffcients $\Delta\mu_{\text{WH-WD}} = 0.73$ cm^{-1} was calculated. It means that, e.g., considering features with a thickness $s = 100$ μm, parallel to the beam direction, the relative difference due the absorption [39] $(\Delta I/I)_{\text{abs}}$ for weddellite and whewellite is equal to 0.008. This value is less than the minimum detectable contrast for absorption ($\approx 1\%$). On contrary, the calculated phase modulation is $\Delta\Phi = 0.1$ rad that corresponds to the contrast of 10%, which is twice larger than the typical minimum detectable contrast due the phase modulation ($\approx 5\%$). As a consequence, in order to get a reliable contrast for these two components and also to visualize further features inside the sample (e.g., the annual ring structure, "Sample 10371"), the measurements were accomplished in an edge-detection regime for phase-contrast μCT. This was realized by optimizing experimentally the sample-to-detector distance to $d_{\text{sample-CCD}} = 50$ cm.

For quantitative analysis, i.e., to evaluate the mineralogical composition of the stones, image segmentation should be applied. The 3D distribution of weddellite, apatite, and whewellite in the whole investigated urinary calculi fragment obtained by SR-μCT quantitative image analysis is shown in "SR-μCT quantitative image analysis". The quantitative analysis has been performed using the Pore3D software library [40] developed by the SYRMEP group at Elettra. The first and most tricky step of the analysis process consists in the segmentation of the images, i.e., the definition of areas representing each mineral constituent (whewellite, weddellite, and apatite). In the present paper, the segmentation has been performed by first applying a manual threshold in order to separate the background from the sample and then using the automatic k-means clustering [41] method for the identification of each mineral constituent.

After segmentation, the assessment of the mass percentage of the different minerals present in the urinary calculi comes straightforward by simply counting the number of voxels belonging to each identified cluster with respect to the total number of voxels (excluding background voxels). These latter values should be finally normalized taking into account the mass density values in order to have mass the percentage measures.

Results and discussion

The employed SR-μCT technique provides information on spatial distribution of minerals within the volume of urinary calculi. Thus, obtained finding makes it possible to analyze initiation of a calculi core formation and a mineral and structural development of the stone in time.

Texture of urinary calculi samples

The texture of the investigated samples (10371, 11727, and 11684) described in "Sample characterization" was obtained non-destructively from the reconstructed SR-μCT slices.

Sample 10371

The investigated specimen is a fragment of a bigger piece which was disintegrated in vivo and then cut in three pieces in vitro. Before the analysis the samples were embedded in Parafilm®. In the SR-μCT slice presented in Fig. 2 of this homogenous urinary calculus a pure whewellite structure is visible.

The visible, concentric, shell-like texture with radial pattern (annual rings) is typical of whewellite in the urinary stones. The layers are formed by plate like-crystals with organic matrix between layers (darker zones in the slice). These layers are more clearly visible on the 3D rendering of the investigated area of the sample.

Sample 11727

This porous spall is crystallic at the surface and exhibits distinctly concentric structure. This type of urinary calculus appears frequently in detritus resulting from breaking of uroliths in vivo. The axial SR-μCT slice in Fig. 3 shows whewellite layers, with mammillary texture. The hiatus between layers contains dry organic material and minute crystals. The concentric structures can be located also on the 3D rendering of this urinary calculus (Fig. 3).

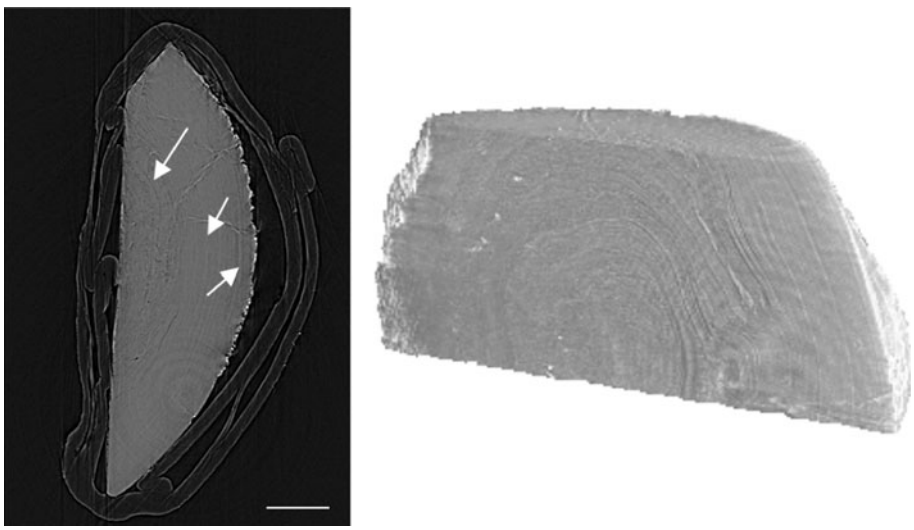

Fig. 2 SR-μCT axial slice of urinary calculi fragment 10371 together with the 3D rendering of the investigated part of the sample, created using 320 axial slices. *Arrows* show some visible annual rings. The ring structure should not be confused with the ring artifact present slightly in the bottom right part of the slice. Around the sample the structure of packing material, the Parafilm® embedding the sample is visible. The *bar* has a length of 1 mm

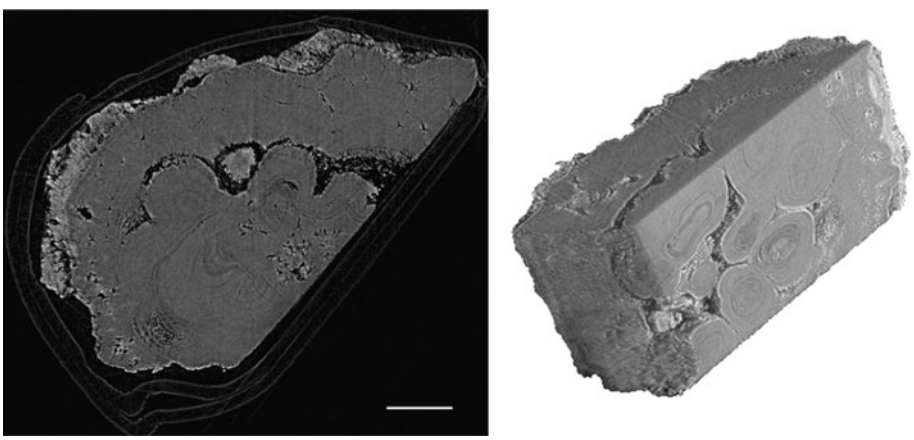

Fig. 3 SR-μCT axial slice of the sample 11727 together with the 3D rendering of the investigated part of this urinary calculi fragment. In the slice the structure of packing material, the Parafilm® embedding the sample is slightly visible. The *bar* has a length of 1 mm

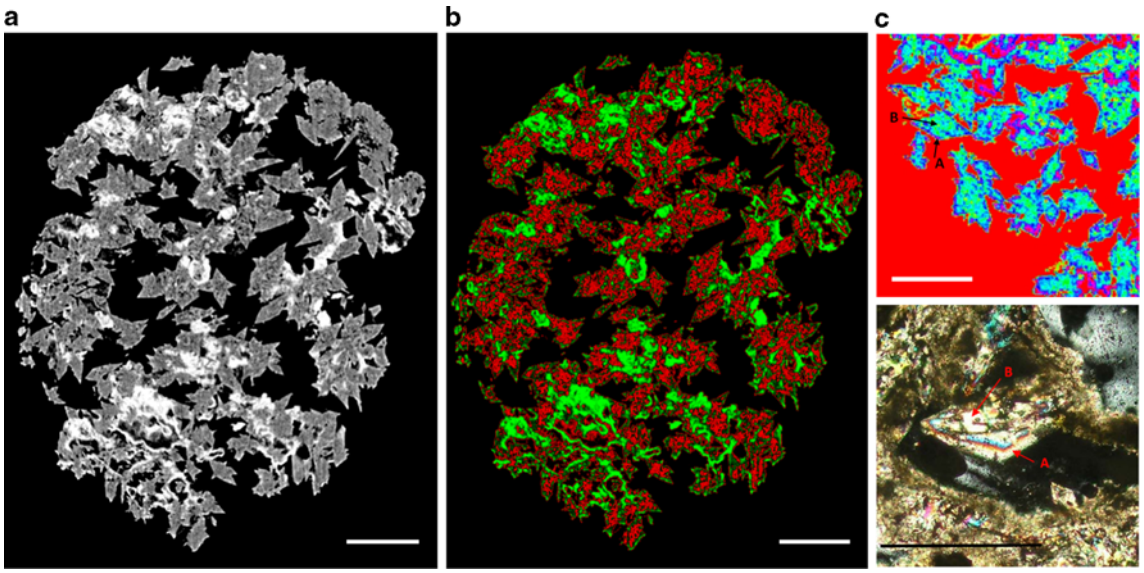

Fig. 4 Axial SR-μCT slices of sample 11847 above the contact of the base of the subsurface crystal layer with the central part of the urinary calculus: **a** and **b** show, respectively, **a** raw and **b** the corresponding *colored slice*; **c** *upper image*: detail of another SR-μCT slice shown in "spectrum" lookup table in order to visualize the secondarily formed whewellite crystals (*greenish-blue color B*) together with the rest of weddellite crystals (*blue A*), in comparison with the PM image of a weddellitte crystal (*A*) with a new whewellite crystal (*B*) in the middle (*lower image*). The *interferential colors* of weddellite (*A*) are more flaring then those of whewellite (*B*). The *bars* have a length of 1 mm

Sample 11847

This sample, due to its structure in which all minerals typical for calcium oxalate-based urinary calculus are present, was investigated in more details. It was measured twice by SR-μCT technique. The results of SR-μCT were compared with the outcomes of standard approaches.

Cross-sections perpendicular to crystal growth direction The axial SR-μCT slices of this urinary calculus (Fig. 4a) show a porous irregular texture. Cross-sections of weddellite bipyramids dominate. These Cross-sections are more granular in the center than near the surface of the sample (lower part of Fig. 4a). This is caused by the higher level of dehydration in the central parts of the urinary calculus and by transformation of weddellite into whewellite. White areas represent the occurrence of apatite. Due to high contrast, apatite (light green color) is also evident in the Fig. 4b), where the lookup table "red-green" was selected. It is deposited irregularly; either it fills the pores among oxalates, or forms layers. It should be noted that using this lookup table we cannot distinguish between weddellite and whewellite in the sample.

The new, i.e., secondarily formed crystals of whewellite from weddellite are emphasized in Fig. 4c). In the SR-μCT slice detail shown in "spectrum" lookup table blue represents the rest of weddellite and greenish-blue the formed whewellite crystals. This typically idiomorphic irregular weddellite crystal texture with different gradual stages of transformation into whewellite [42] is also visible on the polarizing microscopy (PM) image of the same structure in the sample. This figure shows a weddellite crystal with a new whewellite crystal in the middle.

Cross-sections parallel to crystal growth direction The features of texture observable on SR-μCT slices obtained from sample embedded in resin are compared to the images of nearby cross-sections acquired by PM and by SEM.

In the details of SR-μCT slice, SEM and PM images (Fig. 5) the appropriate visualizations of weddellite crystals (A), secondary whewellite crystals (B) and fine-grained textures of apatite (C) are shown. The mosaic texture of whewellite crystals originated from weddellite and the rest of weddellite on the tip of dendrite are clearly visible in all three images. Fine-grained texture of apatite is shown by white color for SR-μCT and SEM images. On PM images obtained by the crossed nicols the fine grained apatite is black.

SR-μCT quantitative image analysis

The quantitative analysis of the digital volumes of sample 11847 (Fig. 6) has been carried out on the whole reconstructed volume as well as on two cropped volumes of about 2.5 mm^3 in order to consider volumes similar to those considered by the infrared analysis (IRS).

Table 3 reports the computed values for the sample 11847. It must be underlined that the computed values are strongly related to the segmentation step and slightly to the

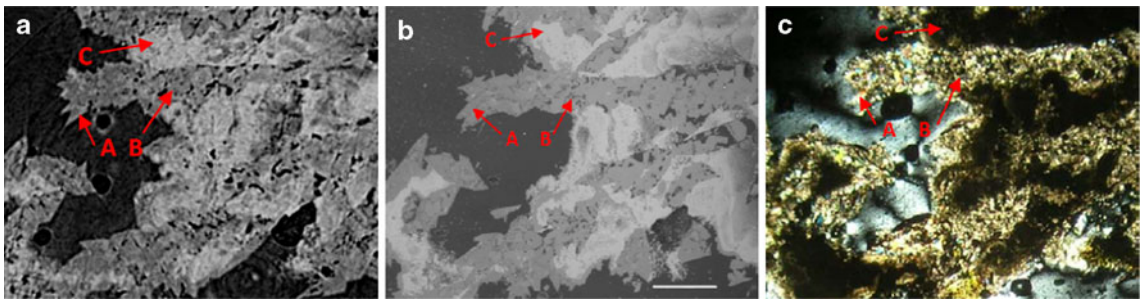

Fig. 5 Comparison of texture details on **a** SR-μCT slice, **b** SEM and **c** PM images. *A* weddellite crystals, *B* secondary whewellite crystals and *C* fine grained textures of apatite. The *bar* has a length of 0.5 mm

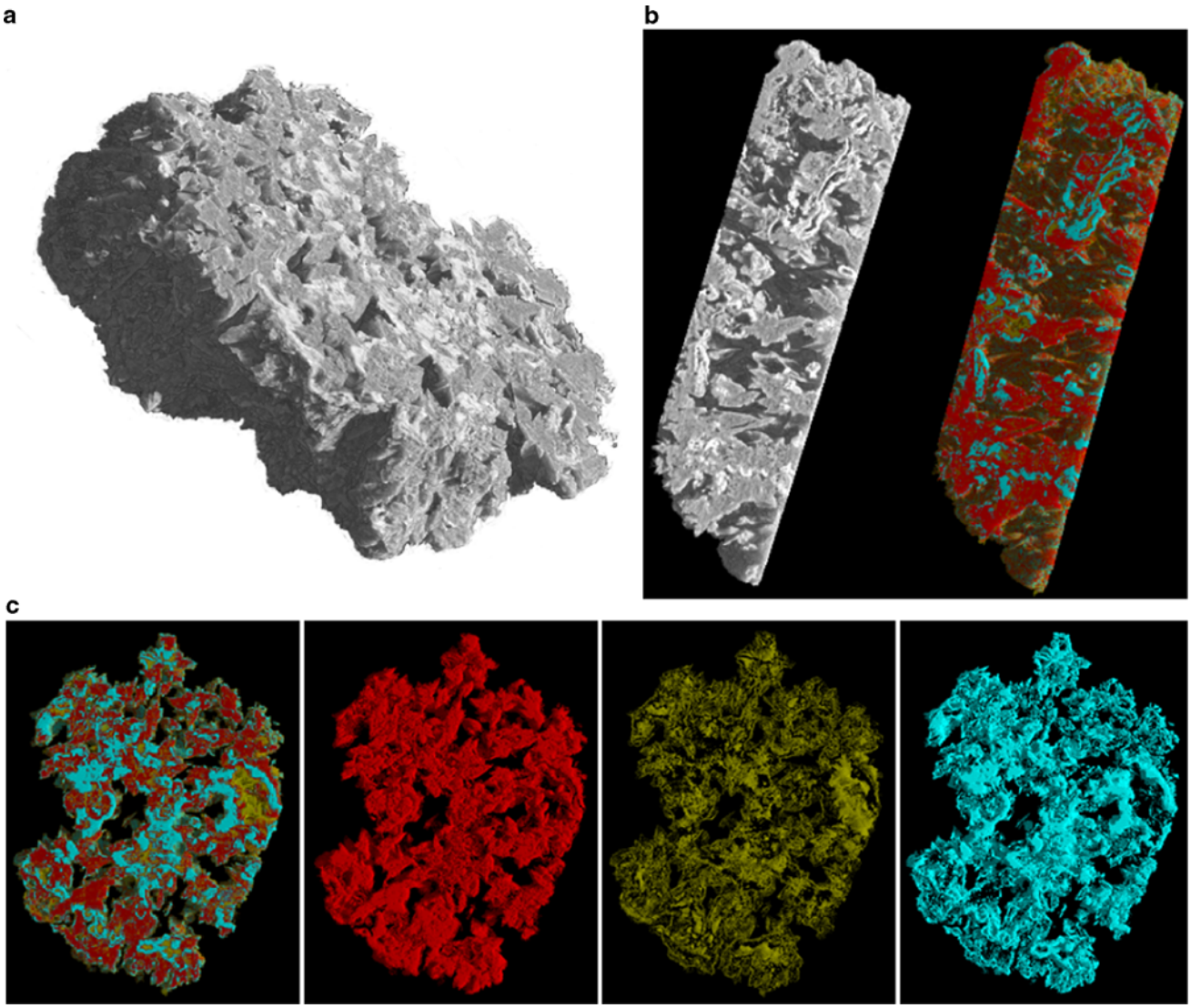

Fig. 6 The outcomes from 3D quantitative analysis for the investigated 11847 urinary calculi fragment. **a** 3D rendering of the measured part of the sample together with **b** a crop 451 × 732 × 182 pixels of the sample shown in *grayscale* and using *virtual colors*, respectively; **c** 3D rendering showing the segmentation of 20 slices with the three different components: whewellite (*red*), weddellite (*yellow*) and apatite (*blue*)

volume considered. While in the present paper an automatic segmentation procedure was preferred, a manual segmentation (for instance segmentation by thresholding with user-supervised thresholds) may be applied resulting in slightly different results. It should be also noted that the precision of IRS analysis is ±10%.

Table 3 Computed values of minerals present in the investigated sample

11847	Crop_1	Crop_2	Whole stack	IRS results
Whewellite (%)	15.9	15.2	14.9	20
Weddellite (%)	50.5	51.1	52.7	45
Apatite (%)	33.6	33.7	32.4	35

The results obtained from the IRS analysis are shown for comparison

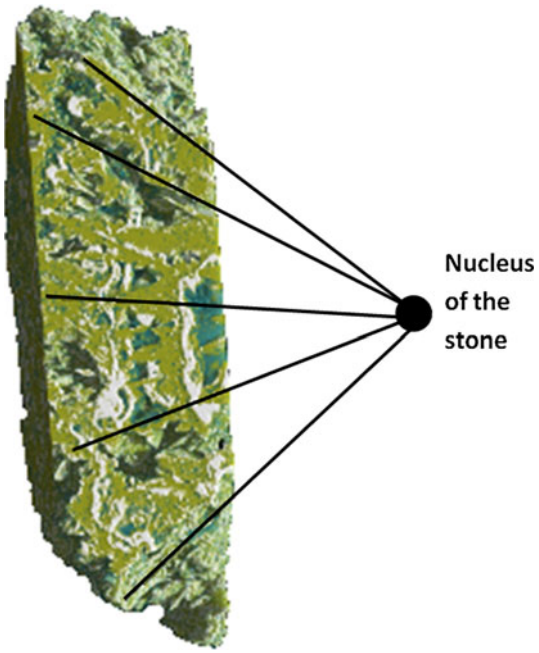

Fig. 7 Determination of the urinary calculi nucleus from segmented volume of the measured calculi fragment

Apart from the quantification of components, the segmented 3D sections also allow to derive further information about the sample microstructure. As an example the localization of the stone nucleus is shown in Fig. 7.

The nucleus of the stone is lying out of the section measured by SR-μCT. The radial coarse-grained texture produced by bipyramidal crystals of weddellite is the main characteristic of this sample. The apatite (white), which is often accompanied by layers of whewellite, is arranged by continuous layers or it coats weddellite bipyramids and fills up the pores among the weddellite crystals. The layers of apatite are concentric and correspond with the change in the condition of crystallization.

Conclusion

This work demonstrated the capabilities of SR-μCT analysis for non-destructive highly spatially resolved analysis of mineralogical composition of urinary calculi samples. This technique is convenient for study of selected urinary calculi formation and reconstruction of temporal evolution of its growth in the organism of patients, even in the case when only a sample fragments disintegrated in vivo are available. The results also show that non-destructive determination of urinary calculi mineralogical composition from reconstructed SR-μCT slices is in a good agreement with results obtained by the current analytical methods. Moreover, SR-μCT analysis allows choosing the optimal cutting planes within the given sample for the subsequent local chemical analysis.

Acknowledgments We acknowledge the Ministry of Education, Youth and Sports of the Czech Republic for bestowing the research project OC09013 and MSM0021622412 and the support by the European Community—Research Infrastructure Action under the FP6 "Structuring the European Research Area" Programme (through the Integrated Infrastructure Initiative "Integrating Activity on Synchrotron and Free Electron Laser Science"). We acknowledge Czech Science Foundation for bestowing the grant project 203/09/1394. J. K. acknowledges Central European Initiative (CEI) for CERES fellowship. Special thanks to Kateřina Proksová and Hana Nováková for their help with SR-μCT measurements and data processing, and to Jaromír Leichmann for help with mineralogical documentation.

References

1. Pramanik R, Asplin JR, Jackson ME, Williams JC Jr (2008) Protein content of human apatite and brushite kidney stones: significant correlation with morphologic measures. Urol Res 36:251–288
2. Herring LC (1962) Observations on the analysis of ten thousand urinary calculi. J Urol 88:45–562
3. Mandel NS, Mandel GS (1989) Urinary tract stone disease in the United States veteran population. Geographical analysis of variations in composition. J Urol 142:1516–1521
4. Bon D, Dore B, Irani J, Marroncle M, Aubert J (1996) Radiographic prognostic criteria for extracorporeal shock-wave lithotripsy: a study of 485 patients. Urology 48:556–560
5. Williams CJ Jr, Sav KC, Paterson RF, Hatt EK, McAtter JA, Lingeman JE (2003) Variability of renal stone fragility in shock wave lithotripsy. Urology 61:1092–1096
6. Taton G, Rokita E, Wróbel A, Beckmann F, Thor P, Worek M (2009) Analysis of renal calculi structure with the use of X-ray microtomography. In: Dössel O, Schlegel WC (eds) IFMBE Proceedings 25/IV, Springer, Berlin, pp 382–385
7. Chaudhri MA, Watling J, Khan FA (2007) Spatial distribution of major and trace elements in bladder and kidney stones. J Radioanal Nucl Chem 271:713–720
8. Cifuentes Delatte L (1977) Study of calculi structure using thin mineralogical section. J Urol Nephrol 83(2):592–596
9. Daudon M, Bazin D, André G, Jungers P, Cousson A, Chevallier P, Véron E, Matzen G (2009) Examination of whewellite kidney stones by scanning electron microscopy and powder neutron diffraction techniques. Appl Cryst 42:109–115
10. Daudon M, Jungers P, Bazin D (2008) Peculiar morphology of stones in primary hyperoxaluria. New Engl J Med 359:100–102
11. Zvara VL, Revúsová V (1988) Močové konkrementy (Urinary calculi). Veda SAV, Bratislava
12. Kageyama S, Kuwahara M, Kurosu S, Orikasa S (1986) Computer tomography and urinary calculi. 2. Determination of the

composition of calculi by the CT value. Nippon Hinyokika Gakkai Zasshi 77:289–294
13. Kageyama S, Kuwahara M, Kurosu S, Orikasa S (1984) Computer tomography and urinary calculi. 1. Clinical evaluation of intrarenal microlith. Nippon Hinyokika Gakkai Zasshi 75:619–623
14. Williams CJ Jr, Zarse CA, Jakckson ME, Witzmann FA, McAteer JA (2006) Variability of proteine contenting calcium oxalate monohydrate stones. J Endourol 20:560
15. Becker-Gaab C, Perouansky M, Zrenner M, zur Nieden J (1986) Sonographic diagnosis of kidney calculi-comparative study of ultrasound, excretory urography and computer tomography in 310 patients. Digitale Bilddiagn 6:128–134
16. Gaucher O, Hubert J, Blum A, Regent D, Mangin P (1998) Evaluation of spiral computed tomography in the demonstration of kidney stones. Ex vivo study. Prog Urol 8:347–351
17. Navarro Sánchez-Ortiz A, Fernández Mena FJ, Zuluaga Gómez A, Aguilar Ruiz J (1989) Densitometric study of staghorn lithiasis using computerized tomography. Arch Esp Urol 42:539–544
18. Davidson MT, Batchelar DL, Velupillai S, Denstedt JD, Cunningham IA (2005) Laboratory coherent-scatter analysis of intact urinary stones with crystalline composition: a tomographic approach. Phys Med Biol 50:3907–3925
19. Grosjean R, Sauer B, Guerra RM et al (2008) Characterization of human renal stones with MDCT: advantage of dual energy and limitations due to respiratory motion. AJR Am J Roentgenol 190:720–728
20. Boll DT, Patil NA, Paulson EK et al (2009) Renal stone assessment with dual-energy multidetector CT and advanced postprocessing techniques: improved characterization of renal stone composition pilot study. Radiology 250:813–820
21. Lam HS, Lingeman JE, Russo R, Chua GT (1992) Stone surface area determination techniques: a unifying concept of staghorn stone burden assessment. J Urol 148:1026–1029
22. Komlev VS, Mastrogiacomo M, Peyrin F, Cancedda R, Rustichelli F (2009) X-ray synchrotron radiation pseudo-holotomography as a new imaging technique to investigate angio- and microvasculogenesis with no usage of contrast agents. Tissue Eng Part C Methods 15:425–430
23. Galiová M, Kaiser J, Novotný K, Samek O, Reale L, Malina R, Páleníková K, Liška M, Čudek V, Kanický V, Otruba V, Poma A, Tucci A (2007) Utilization of laser induced breakdown spectroscopy for investigation of the metal accumulation in vegetal tissues. Spectrochim Acta B 62:1597–1605
24. Kaiser J, Samek O, Reale L, Liška M, Malina R, Ritucci A, Poma A, Tucci A, Flora F, Lai A, Mancini L, Tromba G, Zanini F, Faenov A, Pikuz T, Cinque G (2007) Monitoring of the heavy-metal hyperaccumulation in vegetal tissues by X-ray radiography and by femto-second laser induced breakdown spectroscopy. Microsc Res Tech 70:147–153
25. Farrell AP, Hodaly AH, Wang S (2000) Metal analysis of scales taken from arctic grayling. Arch Environ Toxicol 39:515–522
26. Flem B, Moen V, Grimstvedt A (2005) Trace element analysis of scales from four populations of Norwegian Atlantic Salmon (*Salmo salar l.*) for stock identification using laser ablation inductively coupled plasma mass spectrometry. Appl Spectrosc 59:245–251
27. Kaiser J, Holá M, Novotný K, Hahn D, Diwakar P, Malina R, Galiová M, Kanický V, Liška M (2009) LIBS and LA-ICP-MS Complementary Study of Uroliths. In: Proceedings of 2nd North American Symposium on Laser-Induced Breakdown Spectroscopy (NASLIBS 2009), 13–15 July 2009 New Orleans, LA., USA, Mississippi State University, p 102
28. Cloetens P, Barrett R, Baruchel J, Guigay JP, Schlenker M (1996) Phase objects in synchrotron radiation hard X-ray imaging. J Phys D Appl Phys 29:133–146
29. Baruchel J, Buffière JY, Maire E, Merle P, Peix G (2000) X-ray tomography in material science, general principles. Hermes Science Publications, Paris
30. Zarse ChA, McArteer JA, Sommer AJ, Kin SC, Hatt EK, Lingeman JE, Evan AP, Williams JC Jr (2004) Non-destructive analysis of urinary calculi using micro computed tomography. BMC Urology 4. doi:10.1186/1471-2490-4-15
31. Martinec P, Buryška J (2010) Database of the clinical and pacient′s data about urinary concrements "Urolithiasis OKB MNOF 1978–2010". Institute of Geonics Academy of Sciences Ostrava and Municipal Hospital Ostrava—Fifejdy, Dep. Clinical Biochemistry. Czech Science Foundation, Grant project reg. no. 203/09/1394
32. Cloetens P, Pateyron-Salome M, Buffière JY et al (1997) Observation of microstructure and damage in materials by phase sensitive radiography and tomography. J Appl Phys 81:5878–5886
33. Kak AC, Slaney M (1988) Principles of computerized tomographic imaging. IEEE Press, New York
34. Montanari F, Mancini L, Dreossi D (2003) SYRMEP_Tomo_Project tutorial: Internet Report, Sincrotrone. Trieste, Italy. http://www.ts.infn.it/physics/experiments/syrma/SYRMEP/Tutorial_tomo_program.ppt
35. Abramoff MD, Magelhaes PJ, Ram SJ (2004) Image processing with ImageJ. Biophotonics Int 11:36–42
36. Gerward L, Guilbert N, Jensen KB, Levring H (2001) X-ray absorption in matter. Reengineering XCOM. Radiat Phys chem 60:23–24
37. Gerward L, Guilbert N, Jensen KB, Levring H (2004) WinXCom–a program for calculating X-ray attenuation coefficients. Radiat Phys chem 71:653–654
38. Berger MJ, Hubell JH, Seltzer SM, Chang J, Coursey JS, Sukumar R, Zucker DS, Olsen K (2010) XCOM: Photon Cross Sections Database, Version 1.5. National Institute of Standards and Technology, Gaithersburg, MD. Avaiable at http://physics.nist.gov/xcom. (Originally published as Berger MJ, Hubbell JH (1987) XCOM: Photon Cross Sections on a Personal Computer. National Bureau of Standards (former name of NIST), NBSIR, 87–3597, Gaithersburg, MD)
39. Mancini L, Reiner E, Cloentens P et al (1998) Investigation of structural defects and inhomogeneitites in Al-Pd-Mn icosahedral quasicrystals by combined synchrotron X-ray topography and phase radiography. Philos Mag A 78:1175–1194
40. Brun F, Mancini L, Kasae P, Favretto S, Dreossi D, Tromba G (2010) Pore3D: a software library for quantitative analysis of porous media. Nucl Instrum Methods 615:326–332
41. Hartigan JA (1975) Clustering algorithms. Wiley, New York
42. Schubert G, Brien G, Lenk S, Koch R (1983) Texture examinations on grain and thin section preparations of calcium oxalate calculi and their relations to pathogenetic parameters. Urol Res 11:111–115